CrystEngComm

ROYAL SOCIETY OF CHEMISTRY

PAPER

View Article Online
View Journal | View Issue

Cite this: *CrystEngComm*, 2023, **25**, 5012

Temperature distribution and the laser performance of LD end-pumped LuYSGG/Er:LuYSGG composite crystal

Zhentao Wang,[ab] Dunlu Sun, *[acd] Huili Zhang,[acd] Jianqiao Luo,[acd] Cong Quan,[acd] Zhiyuan Han,[ab] Yang Qiao,[ab] Yuwei Chen[ab] and Maojie Cheng[ac]

In this study, we demonstrate the laser performance of LD end-pumped LuYSGG/Er:LuYSGG composite crystal. Thermal distribution simulations by varying the pump spot size indicate that the suitable pump power density is a key factor affecting the laser performance, which is consistent with the experimental result. The maximum output power and slope efficiency achieved were 1266 mW and 24.3% in CW mode, which increased by 39.3% and 12.5%, respectively, compared with unbonded Er:LuYSGG crystal. The laser wavelength location was at 2797.6 nm, and the power fluctuation was about 5.1%. Moreover, the beam quality factors M_x^2 and M_y^2 improved to 1.33 and 1.42 from 1.78 and 1.83, respectively. The results suggested that an LD end-pumped LuYSGG/Er:LuYSGG composite crystal with a high beam quality can be applied as a seed source in the mid-infrared (MIR) multi-stage amplification laser apparatus.

Received 16th April 2023,
Accepted 26th July 2023

DOI: 10.1039/d3ce00374d

rsc.li/crystengcomm

1. Introduction

Owing to the outstanding performance of laser monochromaticity, high power density, coherence, and variable wavelength, laser can be used in various fields, such as medical surgery, atmospheric monitoring, remote sensing, and military.[1,2] The 2.7–3.0 μm mid-infrared (MIR) laser is worth mentioning due to its strong water absorption band in this range.[3,4] It is well known that the tissues of creatures are very well contented with water, which means that they can absorb laser energy in this wavelength efficiently. Therefore, the 2.7–3.0 μm laser can be used in medical applications, such as surgery.[5] In addition, some nonlinear crystals, such as $ZnGeP_2$ and CdSe, have low absorption loss in the 2.7–3.0 μm waveband, enabling the 2.7–3.0 μm laser to be utilized as an ideal pumping source for optical parametric oscillation (OPO) and optical parametric generation (OPG) to induce mid and far infrared laser operated at 3.0–5.0 μm and 8.0–14.0 μm, respectively.[6]

Some matrix crystals that are suitable for doping with rare earth ions include $Y_3Al_5O_{12}$,[7,8] $YAlO_3$,[9] $Y_3Ga_5O_{12}$,[10] $Gd_3Ga_5O_{12}$,[11] $Y_3Sc_2Ga_3O_{12}$,[12] $Gd_{1.17}Y_{1.83}Sc_2Ga_3O_{12}$,[13] Lu_2O_3, Y_2O_3,[14,15] CaF_2,[16] SrF_2,[17] and $LiYF_4$.[18] Among them, the oxide and sesquioxide crystals are favored by researchers owing to their good chemical stability, excellent mechanical property, and high thermal conductivity.[19,20] The Er^{3+}-doped crystals exhibited distinguished fluorescent properties due to their rich energy level spectral lines, which can be directly pumped to the laser upper level by a commercial InGaAs 970 nm laser diode (LD) and generate the 2.7–3.0 μm laser. This characteristic is beneficial to avoid unnecessary energy loss during the energy-transferring process and thus can improve the laser efficiency.[21] In addition, its unique energy level structure allows it to achieve high-efficiency laser output beyond the Stokes limit through the cooperative up-conversion of the Er^{3+}–Er^{3+} (CU_2) process.[22] However, the laser performance of Er^{3+}-doped crystals is restricted by the severe self-termination effect caused by the long lifetime of the laser lower level. The approach to mitigating self-termination is to increase the doping concentration of the Er^{3+}, but the consequence is the reduction of thermal conductivity. For example, the thermal conductivity of LuYSGG crystals changes from 4.79 to 3.42 W m^{-1} K^{-1} when the doping concentration of Er^{3+} increases from 0 to 30 at%.[23,24]

As stated above, the thermal conductivity of pure matrix crystals is higher than that of doped crystals, enabling them to be bonded as end-caps to increase the heat dissipation capability of doped laser crystals. Chen *et al.* reported that the laser performance of a GYSGG/Er,Pr:GYSGG with a lower maximum temperature obtained from simulation is better than that of Er,Pr:GYSGG.[25] Zhang *et al.* achieved the best

[a] *Crystal Lab of Laser Technology Research Center, Anhui Institute of Optics and Fine Mechanics, Hefei Institutes of Physical Science, Chinese Academy of Sciences, Hefei, 230031, P. R. China. E-mail: dlsun@aiofm.ac.cn*
[b] *University of Science and Technology of China, Hefei, 230026, P. R. China*
[c] *Advanced Laser Technology Laboratory of Anhui Province, Hefei, 230037, P. R. China*
[d] *Key Laboratory of Photonic Devices and Materials, Anhui ProvinceHefei, 230031, PR China*

average power of 20.76 W and M^2 factors of 6.80/6.74 on the LD side-pumped LuYSGG/Er:LuYSGG/LuYSGG bonding rod.[26] Dong *et al.* achieved a maximum power of 909 mW and M^2 factors of 1.78/1.83 on the LD end-pumped Er:LuYSGG crystal.[27] However, for further improvement on the beam quality, the LD end-pumping was combined with thermal bonding technology on the Er:LuYSGG crystal. In addition, the Er:LuYSGG crystal has been proven to be an excellent radiation-resistant laser gain medium.[28]

In this study, the laser performance of LD end-pumped LuYSGG/Er:LuYSGG composite crystal was demonstrated. The effects of the pumping laser spot size and LuYSGG crystal length on temperature distributions were also simulated and analyzed. The results of laser output powers at different pumping laser spot sizes, continuous wave (CW), and pulsed modes were investigated, and the results were compared with the single Er:LuYSGG crystal. The laser spectrum, power stability, and beam quality were also measured.

2. Experiment setup

A 30 at% Er:LuYSGG single crystal with a dimension of about Φ 25 × 105 mm^3 was grown successfully along the <111> orientation using the Czochralki (Cz) method.[27] First, a Φ 25 × 7 mm^3 Er:LuYSGG crystal and Φ 25 × 2 mm^3 LuYSGG crystal were polished precisely and then optically contacted and thermally bonded, respectively. Finally, the composite LuYSGG/Er:LuYSGG crystal bulk with a size of 2 × 2 × 9 mm^3 was prepared for the laser experiment. As exhibited in Fig. 1, a parallel plane resonator cavity with a length of 12 mm was installed to investigate the laser performance. The LuYSGG/Er:LuYSGG crystal was encased with indium foil and fixed into a copper heat sink with cooling water circulated at a temperature of 15 °C for heat dissipation. The 969 nm LD with CW and pulsed modes was used as the pumping source, and the pumping laser was collimated and focused on the bonding surface of the composite crystal by a coupling system. The flat CaF_2 input mirror (M1) was coated with a 970 nm high transmission (HT) film and a 2700–3000 nm high reflection (HR) film. The CaF_2 output mirrors (M2) were coated with the transmittance of 0.5%, 2%, 5%, or 10% of 2790 nm. One more mirror with 970 nm HT and 2700 nm HR films was posited at the end of the optical system to filter the pumping laser and reflect the output laser into the power meter (OPHIR 30A-BB-18). The laser spectrum was measured using a Fourier spectrometer (Thermo Fisher Nicolet iS50) with a spectral interval of 0.5 nm. The laser beam profile and M^2 factor were collected with a pyroelectric array camera (Ophir-Spiricon PY-III-HR).

3. Results and discussion

3.1. Thermal distribution simulation

The heat deposition during laser crystal operation is a non-uniform heat distribution along the radial direction, which leads to different refractive indices of the crystal at various locations, resulting in more critical thermal effects and cutting down the output performance of the laser medium. The finite element method was utilized to analyze the thermal distribution inside the crystal for the better understanding of the effects of different bonding section

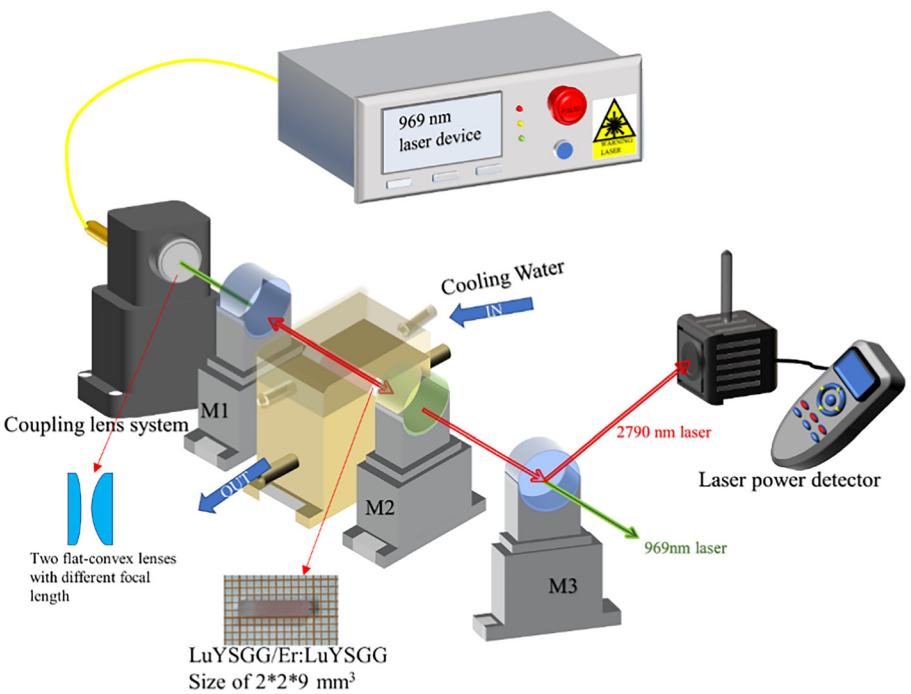

Fig. 1 Schematic experimental setup of LD end-pumped LuYSGG/Er:LuYSGG composite crystal.

lengths and pumping spot sizes on the thermal lensing effect efficiently. When the pumping laser was incident along the geometric center of the end face of the LuYSGG/Er:LuYSGG composite crystal, the thermal model with constant edge temperature is shown in Fig. 2.

When establishing the thermal model, it was assumed that the pumping laser has an ideal Gaussian distribution and was incident along the center of the crystal end-face. The temperatures of the crystal aspects were the same as the cooling block because of close contacting. The two end-faces of the crystal were in contact with air, causing heat exchange between the end-faces and the air, which is much smaller than that from the crystal sides. Therefore, it can be presumed that the two end-faces of the crystal met the following boundary conditions equations:

$$\begin{cases} u(0,y,z) = 288.15\ \text{K};\ u(a,y,z) = 288.15\ \text{K}; \\ u(x,0,z) = 288.15\ \text{K};\ u(x,b,z) = 288.15\ \text{K}; \end{cases} \tag{1}$$

$$\left.\frac{\partial u(x,y,z)}{\partial z}\right|_{z=0} = 0;\ \left.\frac{\partial u(x,y,z)}{\partial z}\right|_{z=c} = 0. \tag{2}$$

Considering that the temperature rise of the composite crystal cannot be infinite, the temperature distribution of the composite crystal in different regions needs to satisfy the bounded conditions:

$$u_1(x, y, z)|_{z=d} < +\infty; \tag{3}$$

$$u_2(x, y, z)|_{z=d} < +\infty. \tag{4}$$

For LuYSGG/Er:LuYSGG composite bulk, the thermal bonding technique allows permanent bonding of LuYSGG and Er:LuYSGG crystals without the need for additional bonding agents when the conditions of continuous temperature and heat flow density should meet on the dividing surface of the two crystal materials:

$$u_1(x, y, z)|_{z=d} = u_2(x, y, z)|_{z=d}; \tag{5}$$

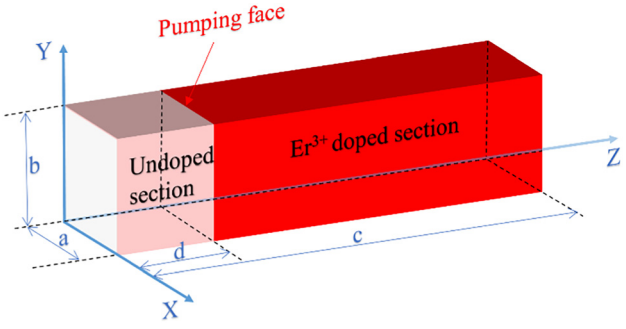

Fig. 2 Schematic structure of LD end-pumped LuYSGG/Er:LuYSGG composite crystal bulk.

$$K\left.\frac{\partial u_1(x,y,z)}{\partial z}\right|_{z=d} = K\left.\frac{\partial u_2(x,y,z)}{\partial z}\right|_{z=d}. \tag{6}$$

The laser crystal has an internal heat source and follows the Poisson equation for heat conduction:

$$K_x\frac{\partial^2 u}{\partial x^2} + K_y\frac{\partial^2 u}{\partial y^2} + K_z\frac{\partial^2 u}{\partial z^2} = -Q(x,y,z), \tag{7}$$

where u represents the internal temperature field of the crystal, K is the heat conduction coefficient of the three axes of the crystal (where the three are equal), and $Q(x, y, z)$ is the heat source, and its expression is:

$$Q(x,y,z) = \frac{2P_{\text{in}}\alpha\eta}{\pi\omega_P^2}\exp(-\alpha z)\cdot\exp\left(-\frac{x^2+y^2}{\omega_P^2}\right), \tag{8}$$

where P_{in} and ω_{P} are the power and spot size of the pumping light, α is the absorption coefficient of the crystal to the pumping light, $\eta = \frac{\lambda_{\text{L}} - \lambda_{\text{P}}}{\lambda_{\text{L}}}$ is the thermal conversion coefficient measured by the fluorescence quantum effect and internal loss, λ_{P} is the LD emitting laser wavelength, and λ_{L} is the excitation laser wavelength of resonant cavity oscillation.

The effects of different bonding section lengths on the temperature distribution inside the crystal were simulated and the results are shown in Fig. 3. It is evident from Fig. 3 that composite crystals can significantly reduce the temperature of the laser crystal. When the length of the bonded pure crystal was 1 mm, the maximum temperature at the pump interface was 340.03 K, which is 78.03 K lower than that of the unbonded crystal. However, with the increasing length of the bonded crystal, the temperature rise at the pump surface does not decrease significantly. After studying the effect of other experimental conditions, such as the thermal bonding process, the bulks with a

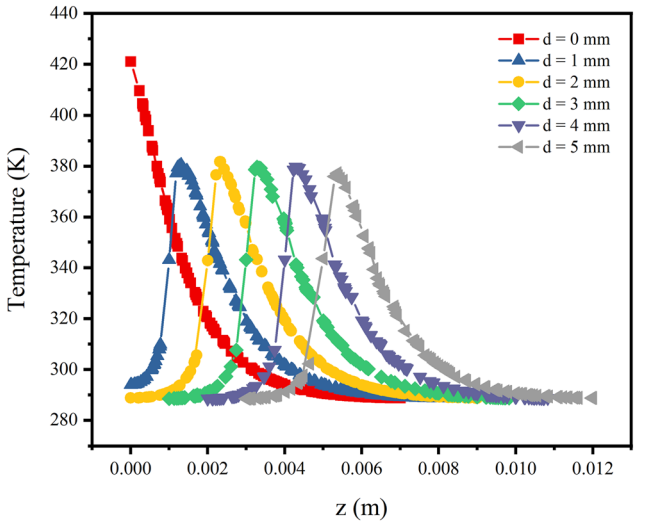

Fig. 3 Temperature along the z-axis of gain crystals bonded to LuYSGG of different lengths.

Table 1 Partial thermodynamic properties of 30 at% of Er:LuYSGG and pure LuYSGG used in the thermal simulation[23,24]

Parameter	Values of Er:LuYSGG	Values of LuYSGG
Thermal conductivity	3.432 W m^{-1} K^{-1}	4.79 W m^{-1} K^{-1}
Density	6129.79 kg m^{-3}	5600 kg m^{-3}
Absorption coefficient	856 m^{-1}	0 m^{-1}
Coefficient of thermal expansion	7.91 × 10^{-6} K^{-1}	8.50 × 10^{-6} K^{-1}
Heat capacity	454 J kg^{-1} K^{-1}	553 J kg^{-1} K^{-1}

bonding length of 2 mm were used in the laser experiments (Table 1).

In addition, we investigated the effect of different pumping spot sizes on the thermal distribution inside the crystal. For the actual experimental conditions, the input power was set at 6 W, and the pumping spot diameters were 190, 300, and 370 μm. The results are shown in Fig. 4 (a). The first three crystals have a bonding length of 2 mm and incident laser diameters of 370, 300, and 190 μm, respectively, and the rightmost crystal is an unbonded crystal with an incident spot size of 190 μm. The temperature distribution of the four crystals in the incident cross section is shown in Fig. 4(b)–(e). It is clear that as the spot diameter becomes tiny, the input power density becomes greater. As the power density increases, on the one hand, the pumping efficiency will become higher, and on the other hand, more thermal deposition will occur and cause a series of thermal effects. The maximum temperature inside the crystal was 381.79 K for a 2 mm bonded crystal with a pump spot diameter of 190 μm, which is lower than that of the unbonded crystal under the same conditions. This confirms the inextricable link between the thermal distribution inside the crystal and the pump power density.

3.2. Laser performance

Fig. 5 exhibits the laser performance of the CW LD end-pumped LuYSGG/Er:LuYSGG composite crystal at different output mirror transmittances. The maximum output power of 1266 mW was achieved at an output mirror transmittance of 5%, corresponding to the slope efficiency of 24.3% and optical–optical conversion efficiency of 21.1%, respectively. Compared with the un-bonding Er:LuYSGG crystal, the maximum output power and slope efficiency were only 909 mW and 21.6%.[27] After thermal bonding, the two values were increased by 39.3% and 12.5%, respectively, indicating strong evidence that thermal bonding can effectively mitigate the thermal effects. Furthermore, it is noted that the photon oscillation in the cavity will produce transmission loss. As the transmission of the output mirror increases, the loss becomes higher, thus causing the threshold of the laser output to escalate.

In addition, the effect of different pumping laser spot diameters on the output power with the transmittance of 5% is shown in Fig. 6. The LD coupling system is composed of two convex opposing plano-convex lenses, whereby one is the collimating lens with focal lengths of 40 mm, while the other lens is the focusing lens with a focal length of 80, 100, or 120 mm, fixed in a mirror holder. The corresponding magnification ratios (MR) were 1 : 2, 1 : 2.5, and 1 : 3. The spot

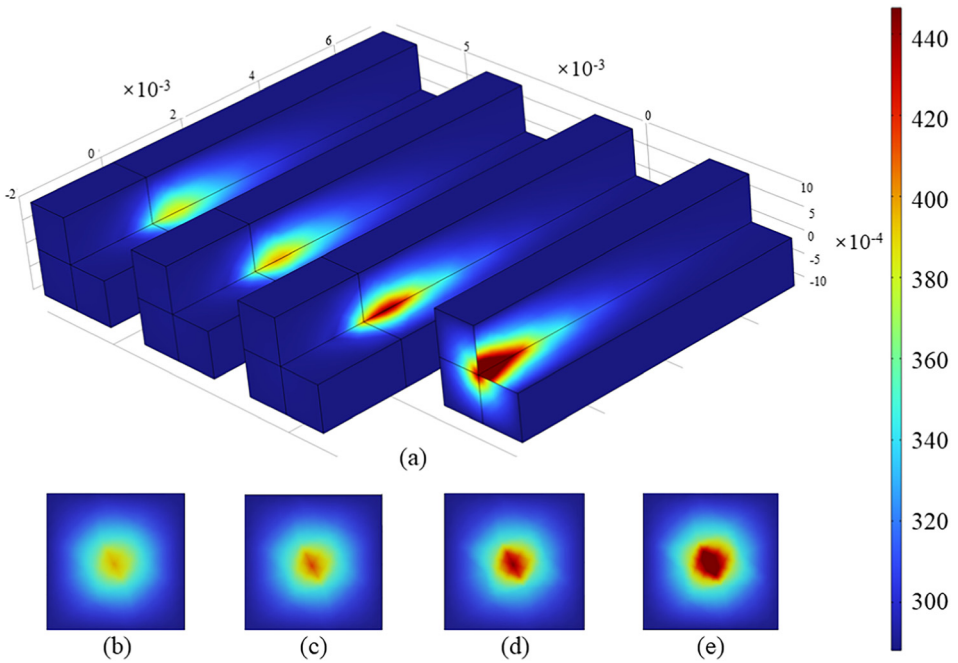

Fig. 4 (a) Shows the schematic of temperature distributions along the *z*-axis inside the crystal at an incident power of 6 W with different pump spot diameters. (b), (c) and (d) represent temperature distribution sections corresponding to the left-to-right bonding surfaces of the crystals in (a) with pump spot diameters of 370, 300, and 190 μm, respectively. (e) Represents single Er:LuYSGG with pump spot diameter of 190 μm.

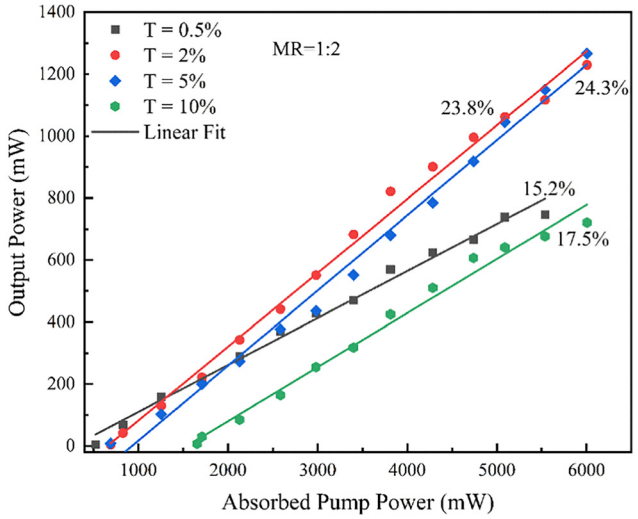

Fig. 5 Laser performance of LD CW end-pumped LuYSGG/Er:LuYSGG composite crystal with different output mirror transmittances.

diameters of 190, 300, and 370 μm were measured using the knife-edge method. The experimental results showed that the maximum output power decreased to 934 and 808 mW with the pumping spot size of 300 and 370 μm, and the saturation has been reached, which is far less than the output power under the same conditions with a pumping spot diameter of 190 μm. It is known that the thermal effect inside the laser crystals at high output power is dangerous, which limits the laser performance of the crystals. As the pump spot size reduces, the power density of the pumping laser increases, which could lead to a heavier thermal effect. However, in this case, the laser performance of the crystal becomes better as the pumping spot diameter becomes smaller, which can be illuminated by the fact that a smaller incident spot leads to a higher pumping power density and excitation efficiency. With

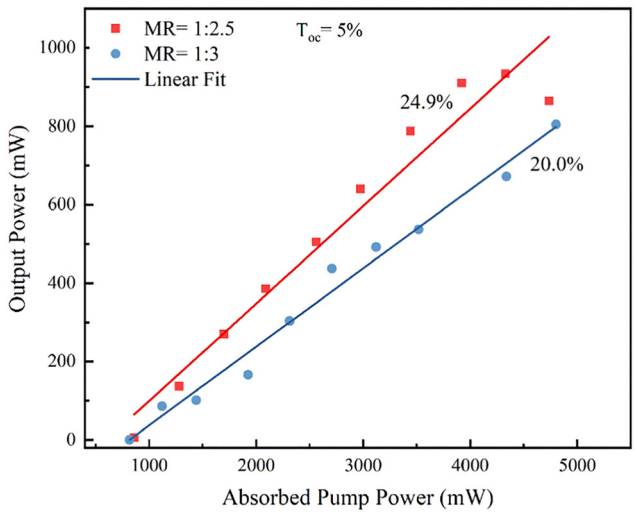

Fig. 6 Laser performance for LuYSGG/Er:LuYSGG crystal bulks under 969 nm LD end-pumping in CW mode with different magnification ratios.

the excellent physicochemical properties of the laser crystal, the reduction of output power due to the thermal effect at this pump power is much less than the increment caused by higher pump power density.

Furthermore, the laser performance of the crystal in pulsed mode at different operating frequencies and pulse widths was investigated. As seen from Fig. 7, when the operating frequency is 200 Hz, the laser slope efficiency increases with the pulse width, and the maximum output power of 973 mW was obtained when the pulse width is 1.8 ms. The fitted data showed that the laser output power does not reach saturation and is lower than that in CW mode, which could be due to the slight thermal effect and incomplete pumping caused by the short duty cycle at low repetition frequencies. When the repetition frequency is 300 Hz, the slope efficiency still increases with the increase of pulse width, and the laser output power of 1031 mW and the slope efficiency of 24% are obtained at 1.8 ms. This can be considered as the optimal LD end-pumped pulse mode condition for the laser output at a size of 2 × 2 × 9 mm^3 of composite LuYSGG/Er:LuYSGG crystal bulks. When the frequency reaches 400 Hz, with the increment of the pulse width, the slope efficiency changes a little, and the maximum output power decreases. Meanwhile, under the condition of 500 Hz, the slope efficiency shows a decreasing trend, and the maximum output power at each pulse width condition is lower than that under the condition of 400 Hz. The laser output power also tends to saturate readily due to the duty cycle that is higher under this circumstance, resulting in a more significant thermal effect that limits the laser performance of the crystal.

Under the same experimental conditions, the laser performance of LD end-pumped Er:LuYSGG crystal bulks with the size of 2 × 2 × 7 mm^3 was also investigated and compared with the bonded one. We can see from Fig. 8 that a maximum output power of 567 mW with a slope efficiency of 17.7% was obtained at a repetition frequency of 300 Hz and a pulse width of 1.2 ms. However, a maximum laser output of 959 mW with a slope efficiency of 22.2% under these conditions was achieved by the LD end-pumped LuYSGG/Er:LuYSGG composite crystal, which is an improvement of 69.1% and 25.4% for both values. Besides, when the pulse frequency was 300 Hz and the pulse width of 1.8 ms, which is the optimal output condition for the bonded crystal, the maximum output power and slope efficiency of the single Er:LuYSGG were only 376.1 mW and 13.3%, respectively, corresponding to the improvements of 174.2% and 44.4% by bonding technology. The reason for the poor laser performance of single Er:LuYSGG is that operation at high duty cycle results in heavy heat deposition due to its relatively low thermal conductivity, which leads to severe thermal effects, thus degrading the laser performance. The bonding technology highly improves the thermal management ability of the crystal to the point that it can withstand higher pumping energies without mechanical

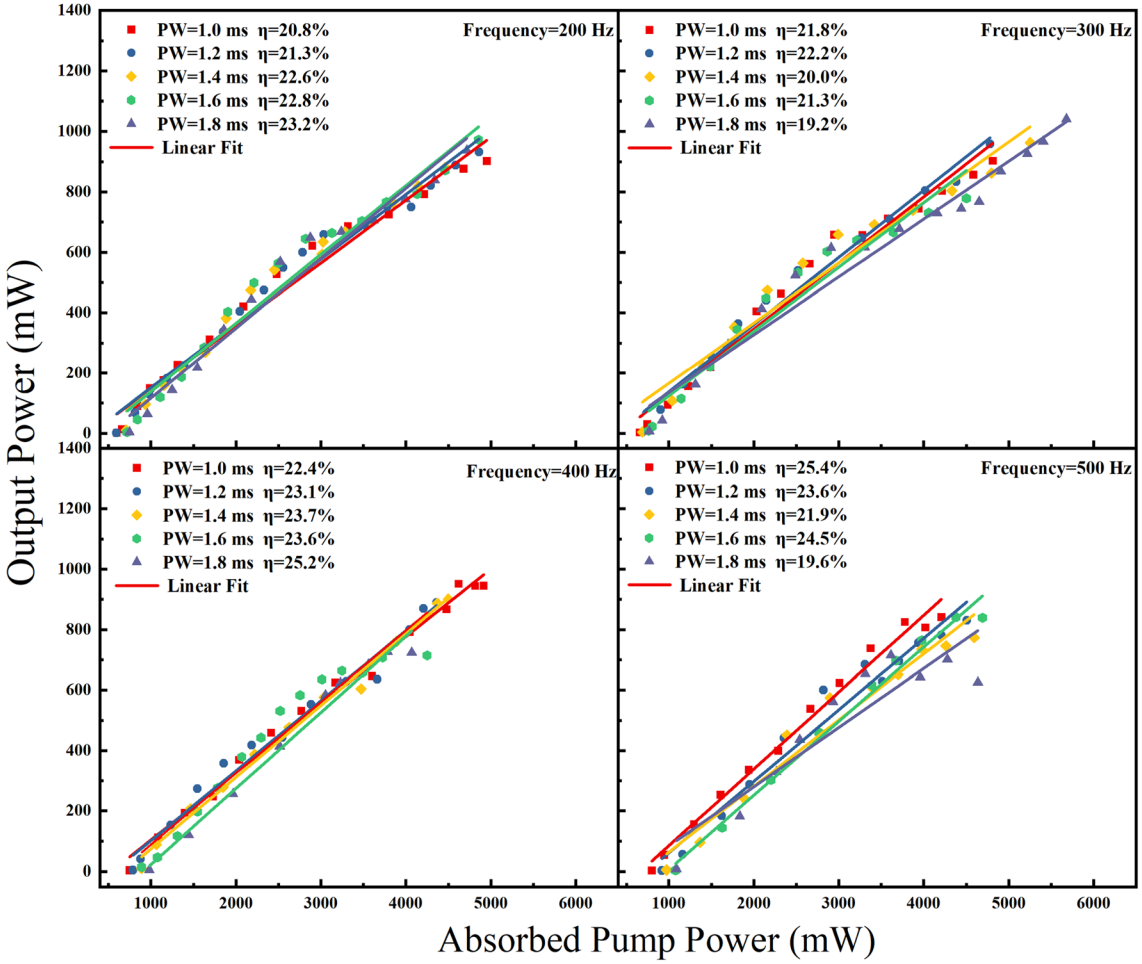

Fig. 7 Laser performance of 969 nm LD end-pumped Er:LuYSGG crystal bulks at different frequencies and pulse widths.

damage, resulting in a higher power laser output by increased adequate pumping.

3.3. Laser stability

The average output power of 584.7 mW was obtained at 60% of the maximum absorbed pump power at 2796 nm. The output power as a function of time within 10 minutes with a time interval of 30 seconds is shown in Fig. 9. The whole experiment was performed with a cooling water temperature of 15 °C, an output mirror with a transmittance of 5% at 2.79 μm and pump spot diameter of 190 μm in CW mode. It can be seen from Fig. 9 that the maximum output power is 601 mW, which is 30 mW higher than the minimum output power of 571 mW. The power fluctuation of ~2.79 μm was about 5.1%, demonstrating better laser stability. For the future, we look to improve the crystal growth process and crystal processing technology to obtain high quality crystal components and to achieve better laser performance. Moreover, a more durable and stable laser output is expected to be realized by optimizing the size of the laser crystal and improving the thermal management.

3.4. Laser Spectrum

The laser spectrum of the LD end-pumped LuYSGG/Er:LuYSGG composite crystal at an absorbed pump power of 1.34 W is shown in Fig. 10. The central wavelength peak was at 2796.6 nm and the corresponding FWHM was 0.4 nm, suggesting that excellent and stable single-wavelength laser output can be obtained from the LuYSGG/Er:LuYSGG composite crystal.

3.5. Laser beam quality

The beam quality factor is considered an indicator to evaluate the laser performance of the crystal. The experiment was performed in CW pumping mode with an output mirror transmittance of 5% and a cavity length of 12 mm. A CaF_2 convex lens with a focal length of 300 mm was employed to focus the output laser, and the camera was moved away from the lens to record the dimensions of the two axes of the spot "x" and "y" at different positions. The 2D and 3D transverse beam profiles of the LD end-pumped LuYSGG/Er:LuYSGG composite crystal were photographed at an average output power of 800 mW, as shown in Fig. 11. The horizontal and vertical M^2 factors were calculated to be 1.33 and 1.42,

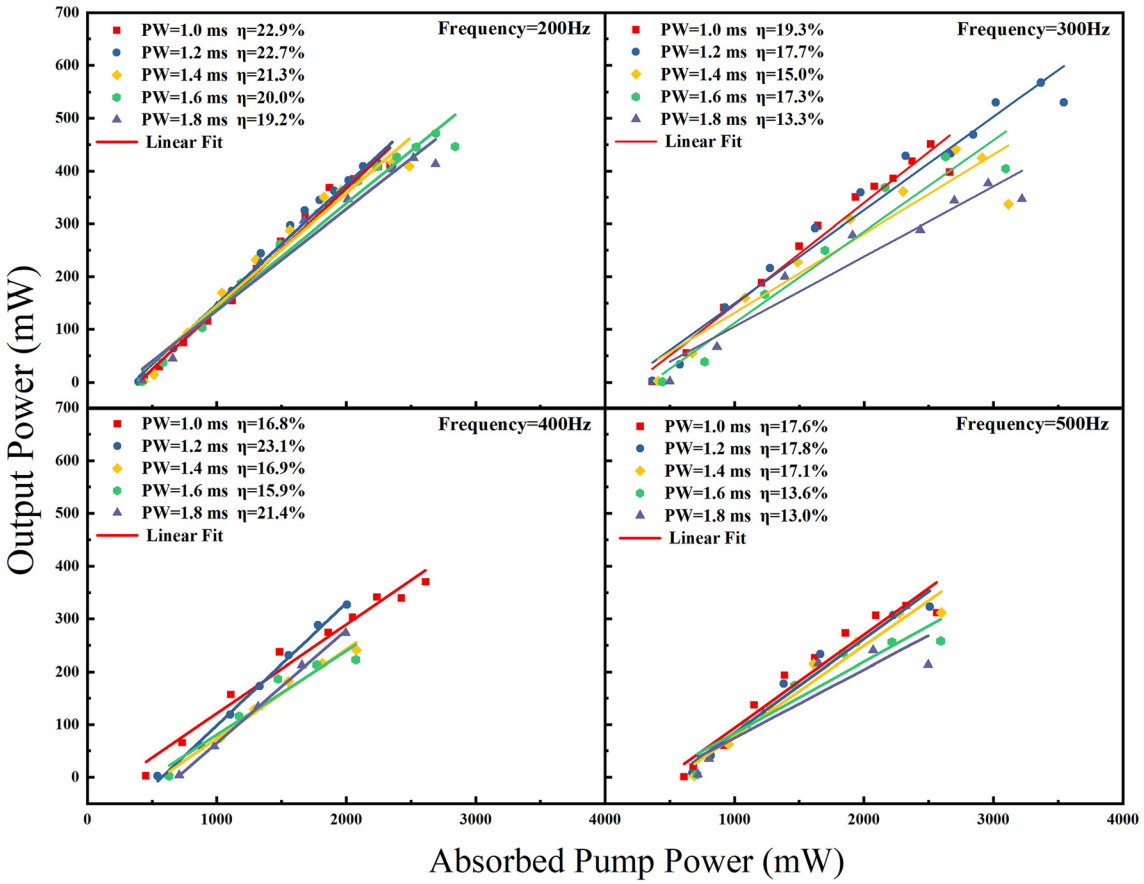

Fig. 8 Laser performance of 969 nm LD end-pumped Er:LuYSGG crystal bulks at different frequencies and pulse widths.

respectively, and the corresponding far-field divergence angles were 18.50 and 18.46 mrad, respectively. Both parameters were reduced compared with the M^2 factors of a single Er:LuYSGG crystal (1.78/1.83),[27] indicating that the bonding technique increases the laser output power and improves the beam quality due to the weakened thermal effect. The result suggests that the LD end-pumped LuYSGG/Er:LuYSGG composite crystal with a high beam quality can be applied as a seed source in the MIR multi-stage amplification laser apparatus.

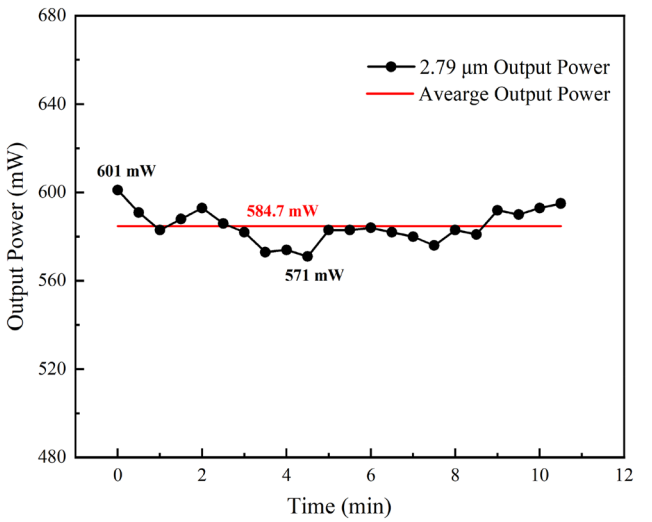

Fig. 9 Laser output power *versus* pumping time was measured at 60% of the maximum absorbed power.

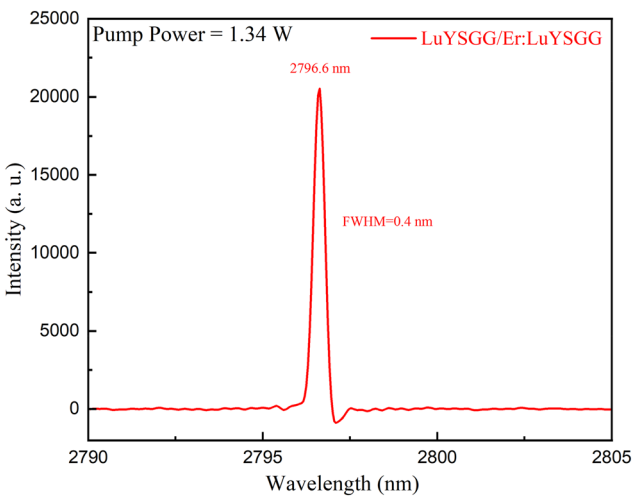

Fig. 10 Laser spectrum of LD end-pumped LuYSGG/Er:LuYSGG composite crystal.

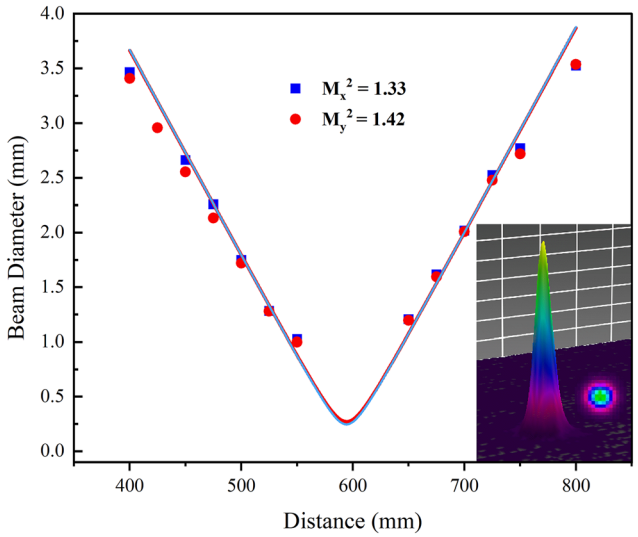

Fig. 11 Laser beam diameter *versus* propagation distance for LuYSGG/Er:LuYSGG composite crystal. Inset: Two-dimensional and three-dimensional beam profiles at an average output power of 800 mW.

4. Conclusion

In this study, the effects of the length of the undoped LuYSGG section and the pump spot diameter on the laser performance of LD end-pumped LuYSGG/Er:LuYSGG composite crystal bulk were investigated. The thermal bonding technique allows the Er:LuYSGG crystal to reduce the maximum temperature at the pumped end-face by 78.03 K during laser operation, but the highest temperature rise of the crystal does not decrease significantly as the unbonded section grows, which can be interpreted as cooling reaches saturation. The thermal distribution simulations showed that suitable pump power density was a significant factor affecting the laser performance, which is consistent with the experimental results. In addition, as the pump spot diameters increased from 190 to 300 and 370 μm, the maximum laser output powers were 1266, 934, and 805 mW, respectively, showing a decreasing trend due to insufficient pump power density. The maximum output power of 1266 mW and slope efficiency of 24.3% in CW mode could be achieved on the LD end-pumped LuYSGG/Er:LuYSGG composite crystal. The optimal pulse conditions were 300 Hz and 1.8 ms, and the output power and slope efficiency obtained under this condition were 1031 mW and 19.2%, respectively. The laser spectrum shows a single wavelength of 2797.6 nm and a corresponding FWHM of 0.4 nm. The laser power fluctuation was about 5.1%, indicating better stability. The beam quality factors M^2 in the "x" and "y" directions were 1.33 and 1.42, which exhibit a better beam quality than that of the un-bonding Er:LuYSGG (1.78/1.83). All the results indicate that the thermal bonding technique can highly strengthen the thermal management capability of an Er:LuYSGG crystal, resulting in improved laser performance at 2.79 μm. Therefore, the LD end-pumped LuYSGG/Er:LuYSGG composite crystal with a high beam quality can be used as a seed source.

Author contributions

Z. T. Wang contributed to the investigation, data curation, and writing-original draft. D. L. Sun contributed to the supervision, writing-review, editing and funding acquisition. H. L. Zhang contributed to the project administration and funding acquisition. J. Q. Luo contributed to the methodology. C. Quan contributed to the funding acquisition and testing. Z. Y. Han contributed to the methodology and software. Y. W. Chen contributed to the writing-review. Y. Qiao contributed to the data curation. M. J. Cheng contributed to the crystal processing.

Conflicts of interest

The authors declared that they have no known competing financial interests or personal relationships that could have appeared to influence the work reported in this paper.

Acknowledgements

This work was financially supported by the National Natural Science Foundation of China (NSFC) (grant no. 52102012), the Hefei Institutes of Physical Science (HFIPS) Director's Fund (Grant No. YZJJ2022QN08), Natural Science Foundation of Anhui Province (Grant No. 2208085QF217).

References

1 W. Krupke, Advanced diode-pumped solid state lasers (DPSSLs): near-term trends and future prospects. *Advanced High-Power Lasers and Applications*, vol. 3888, 2000, SPIE.
2 C. Kränkel, D.-T. Marzahl, F. Moglia, G. Huber and P. W. Metz, Out of the blue: semiconductor laser pumped visible rare-earth doped lasers, *Laser Photonics Rev.*, 2016, **10**, 548–568.
3 C. Labbe, J. L. Doualan, P. Camy, R. Moncorgé and M. Thuau, The 2.8 μm laser properties of Er^{3+} doped CaF_2 crystals, *Opt. Commun.*, 2002, **209**, 193–199.
4 Y. Guo, Y. Tian, L. Zhang, L. Hu, N.-K. Chen and J. Zhang, Pr^{3+}-sensitized Er^{3+}-doped bismuthate glass for generating high inversion rates at 2.7 μm wavelength, *Opt. Lett.*, 2012, **37**, 3387–3389.
5 A. D. Zweig, M. Frenz, V. Romano and H. P. Weber, A comparative study of laser tissue interaction at 2.94 μm and 10.6 μm, *Appl. Phys. B: Lasers Opt.*, 1988, **47**, 259–265.
6 S. W. Hu, L. Wang, Y. W. Guo, T. Q. Cheng, X. Y. Wu, Z. Y. Wang, H. X. Wu, J. Y. Yao, Y. C. Wu and H. H. Jiang, High-conversion-efficiency tunable mid-infrared $BaGa_4Se_7$ optical parametric oscillator pumped by a 2.79 μm laser, *Opt. Lett.*, 2019, **44**, 2201–2203.
7 W. A. Fried, K. H. Chan, C. L. Darling and D. Fried, Use of a DPSS Er:YAG laser for the selective removal of composite

from tooth surfaces, *Biomed. Opt. Express*, 2018, **9**, 5026–5036.

8 H. L. Zhang, X. J. Sun, D. L. Sun, J. Q. Luo, Z. Q. Fang, X. Y. Zhao, C. Quan, L. Z. Hu, M. J. Cheng, Q. L. Zhang and S. T. Yin, Improvement of single pulse energy and laser efficiency by co-doping Cr^{3+} ions into the Er:YAG crystal, *Infrared Phys. Technol.*, 2019, **97**, 197–202.

9 C. Quan, D. L. Sun, J. Q. Luo, H. L. Zhang, Z. Q. Fang, X. Y. Zhao, L. Z. Hu, M. J. Cheng, Q. L. Zhang and S. T. Yin, 2.7 μm dual-wavelength laser performance of LD end-pumped Er:YAP crystal, *Opt. Express*, 2018, **26**, 28421–28428.

10 L. You, D. Lu, Z. Pan, H. Yu, H. Zhang and J. Wang, High-efficiency 3 μm Er:YGG crystal lasers, *Opt. Lett.*, 2018, **43**, 5873–5876.

11 Z. Y. You, Y. Wang, J. L. Xu, Z. J. Zhu, J. F. Li, H. Y. Wang and C. Y. Tu, Single-longitudinal-mode Er:GGG microchip laser operating at 2.7 μm, *Opt. Lett.*, 2015, **40**, 3846–3849.

12 Q. Hu, H. Nie, W. Mu, Y. Yin, J. Zhang, B. Zhang, J. He, Z. Jia and X. Tao, Bulk growth and an efficient mid-IR laser of high-quality Er:YSGG crystals, *CrystEngComm*, 2019, **21**, 1928–1933.

13 X. Y. Zhao, D. L. Sun, J. Q. Luo, H. L. Zhang, Z. Q. Fang, C. Quan, L. Z. Hu, M. J. Cheng, Q. L. Zhang and S. T. Yin, Laser performance of a 966 nm LD side-pumped Er,Pr:GYSGG laser crystal operated at 2.79 μm, *Opt. Lett.*, 2018, **43**, 4312–4315.

14 M. Q. Fan, T. Li, S. Z. Zhao, G. Q. Li, H. Y. Ma, X. C. Gao, C. Krankel and G. Huber, Watt-level passively Q-switched Er:Lu_2O_3 laser at 2.84 μm using MoS_2, *Opt. Lett.*, 2016, **41**, 540–543.

15 Y. S. Zhang, Y. Q. Cai, B. Xu, J. Zhang, L. Xiao, P. Liu and X. D. Xu, Single-mode oscillations of diode-pumped mid-infrared Er:Y_2O_3 ceramic microchip lasers at 2.7 μm, *Opt. Express*, 2019, **27**, 31783–31789.

16 J. Sulc, M. Nemec, R. Svejkar, H. Jelinkova, M. E. Doroshenko, P. P. Fedorov and V. V. Osiko, Diode-pumped Er:CaF_2 ceramic 2.7 μm tunable laser, *Opt. Lett.*, 2013, **38**, 3406–3409.

17 R. Svejkar, J. Sulc, H. Jelinkova, V. Kubecek, W. W. Ma, D. P. Jiang, Q. H. Wu and L. B. Su, Diode-pumped Er:SrF_2 laser tunable at 2.7 μm, *Opt. Mater. Express*, 2018, **8**, 1025–1030.

18 J. Q. Hong, L. H. Zhang, M. Xu and Y. Hang, Effect of erbium concentration on optical properties of Er:YLF laser crystals, *Infrared Phys. Technol.*, 2017, **80**, 38–43.

19 S. Spiekermann, H. Karlsson and F. Laurell, Efficient frequency conversion of a passively Q-switched Nd:YAG laser at 946 nm in periodically poled $KTiOPO_4$, *Appl. Opt.*, 2001, **40**, 1979–1982.

20 B. J. Dinerman and P. F. Moulton, 3-μm CW laser operations in erbium-doped YSGG, GGG, and YAG, *Opt. Lett.*, 1994, **19**, 1143–1145.

21 W. Yao, H. Uehara, H. Kawase, H. Chen and R. Yasuhara, Highly efficient Er:YAP laser with 6.9 W of output power at 2920 nm, *Opt. Express*, 2020, **28**, 19000–19007.

22 V. Lupei, S. Georgescu and V. Florea, On the Dynamics of Population Inversion for 3 μm, Er^{3+} Lasers, *IEEE J. Quantum Electron.*, 1993, **29**, 426–434.

23 K. P. Dong, D. L. Sun, H. L. Zhang, J. Q. Luo, X. Y. Zhao, C. Quan, L. Z. Hu, Z. Y. Han, Y. W. Chen, M. J. Cheng and S. T. Yin, Investigation of defect, mechanical, thermal properties and refractive index on an Er:LuYSGG mixed laser crystal, *Opt. Mater.*, 2021, **121**, 111568–111576.

24 K. P. Dong, D. L. Sun, H. L. Zhang, J. Q. Luo, X. Y. Zhao, C. Quan, L. Z. Hu, Z. Y. Han, Y. Qiao, Y. W. Chen and M. J. Cheng, Growth, physicochemical and optical properties of LuYSGG garnet single crystal, *J. Cryst. Growth*, 2022, **582**, 126522–126530.

25 J. K. Chen, D. L. Sun, J. Q. Luo, H. L. Zhang, S. H. Cao, J. Z. Xiao, H. X. Kang, Q. L. Zhang and S. T. Yin, Performances of a diode end-pumped GYSGG/Er,Pr:GYSGG composite laser crystal operated at 2.79 μm, *Opt. Express*, 2014, **22**, 23795–23800.

26 H. L. Zhang, J. T. Bian, D. L. Sun, J. Q. Luo, C. Quan, L. Z. Hu, Z. Y. Han, K. P. Dong, Y. Qiao, M. J. Cheng and Y. W. Chen, Improvement of 2.8 μm laser performance on LD side-pumped LuYSGG/Er:LuYSGG/LuYSGG bonding crystal, *Opt. Laser Technol.*, 2023, **158**, 108840–108847.

27 K. P. Dong, D. L. Sun, H. L. Zhang, J. Q. Luo, X. Y. Zhao, C. Quan, L. Z. Hu, Z. Y. Han, Y. W. Chen, M. J. Cheng and S. T. Yin, Spectroscopy and LD end-pumped high power 2.79 μm CW laser from an Er:LuYSGG mixed crystal, *J. Lumin.*, 2021, **236**, 118107–118114.

28 H. L. Zhang, J. T. Bian, D. L. Sun, J. Q. Luo, C. Quan, L. Z. Hu, Z. Y. Han, K. P. Dong, M. J. Cheng and Y. W. Chen, Er^{3+}-doped LuYSGG crystal as a potential 2.79 μm radiation-resistant laser material, *Opt. Laser Technol.*, 2022, **152**, 108121–108128.

